Can we relate the surface expression of dike-induced normal faults to subsurface dike geometry?

Craig Magee[1] and Christopher A-L Jackson[2]

[1]School of Earth Science and Environment, University of Leeds, Leeds, LS2 9JT, UK
[2]Basins Research Group (BRG), Department of Earth Science and Engineering, Imperial College, London, SW7 2BP, UK

Many igneous dikes do not reach the surface, instead triggering normal faulting and graben formation in overlying rock. The surface expression of these dike-induced faults provides important records of active and ancient diking. For example, surface measurements of graben half-widths have been used to estimate dike upper tip depths by projecting faults straight down-dip, whereas extension measured at the surface across dike-induced fault pairs (i.e. their cumulative heave) is considered a proxy for dike thickness. We use 3D seismic reflection data to test how the surface expression of two buried, dike-induced faults relates to dike geometry. The dike-induced faults are non-planar, suggesting fault dips should not be assumed constant when using graben half-widths to estimate dike depth. Multiple displacement maxima occur across the dike-induced faults, but rarely at their lower or upper tips, suggesting they formed through linkage of isolated faults that nucleated *between* the dike and free surface. Fault heave is greatest where these subsurface displacement maxima occur, meaning the cumulative heave of the dike-induced fault pair measured at the syn-faulting free surface underestimates their total extension and poorly reflects dike thickness. Our results imply that at-surface analyses of dike-induced fault geometry cannot be used to estimate key

dike parameters without *a priori* knowledge of fault structure and kinematics, or host rock lithological variations.

INTRODUCTION

Dike intrusion can induce normal faulting of overlying rock (e.g., Pollard et al., 1983; Rubin and Pollard, 1988; Rubin, 1992; Xu et al., 2016). Dike-induced normal faults form pairs that dip towards underlying dikes and bound dike-parallel graben (Fig. 1) (e.g., Mastin and Pollard, 1988; Trippanera et al., 2015a; Trippanera et al., 2015b). Faulting occurs because dike dilation concentrates tensile stress in two lobes above the dike upper tip and in two zones at the free surface, within which related shear stresses instigate failure (Fig. 1) (e.g., Pollard et al., 1983; Rubin and Pollard, 1988; Rubin, 1992; Gudmundsson, 2003; Koehn et al., 2019). Because diking drives stress changes promoting faulting, dike emplacement and shape impact fault growth and geometry (e.g., Trippanera et al., 2015a; Dumont et al., 2017). Our understanding of these dike and dike-induced fault relationships has been driven by physical, numerical, and analytical modelling (e.g., Pollard et al., 1983; Mastin and Pollard, 1988; Trippanera et al., 2015b; Hardy, 2016; Bazargan and Gudmundsson, 2019; Koehn et al., 2019). These models help us invert the surface expression of dike-induced faults to: (i) track intruding dikes (e.g., Pallister et al., 2010); (ii) estimate dike volumes (e.g., Wilson and Head, 2002); and (iii) examine how diking controls the morphology of Earth and other planetary bodies (e.g., Wilson and Head, 2002; Carbotte et al., 2006; Ruch et al., 2016). However, few outcrops expose the geometry of *both* dikes and overlying dike-induced faults (e.g., Gudmundsson, 2003; Von Hagke et al., 2019). Without access to the 3D structure of natural dike and dike-induced fault systems, we cannot test models that underpin how we invert surface deformation to estimate dike geometry (e.g., thickness and depth).

We use seismic reflection images of the Exmouth Dyke Swarm, offshore NW Australia (Magee and Jackson, 2020), to quantify the 3D structure of a natural dike and dike-induced fault system. We tested: (i) whether graben half-width can be used to predict dike upper tip depths (e.g., Wilson and Head, 2002; Trippanera et al., 2015b; Hjartardóttir et al., 2016); and (ii) if extension across dike-induced fault pairs measured at the syn-faulting free surface can be considered a proxy for dike thickness (e.g., Rubin and Pollard, 1988; Rubin, 1992; Trippanera et al., 2015b). Our data also informs the debate regarding whether dike-induced faults nucleate: (1) as near-surface vertical fractures (Fig. 1A) (e.g., Trippanera et al., 2015a; Trippanera et al., 2015b; Al Shehri and Gudmundsson, 2018; Von Hagke et al., 2019); (2) at dike tips (Fig. 1B) (e.g., Rubin, 1992; Xu et al., 2016; Koehn et al., 2019); (3) a combination of options (1) and (2) (Fig. 1C) (Tentler, 2005; Rowland et al., 2007); or (4) *between* the dike tip and surface (Fig. 1D) (Mastin and Pollard, 1988; Koehn et al., 2019). These fault growth models can be used to predict diagnostic displacement-depth profiles, if we assume displacement is greatest where faults nucleated (Fig. 1) (e.g., Pollard and Segall, 1987; Trippanera et al., 2015b). Measuring displacement patterns across dike-induced faults may thus reveal their kinematics, which could relate to dike thickness changes and emplacement mechanics. By unravelling how diking translates into faulting, we provide insights into the inversion of dike geometry from surface-based analyses of dike-induced faults.

EXMOUTH DYKE SWARM AND STUDY AREA

Dikes in the Exmouth Dike Swarm manifest in the seismic reflection data as ~NNE-trending, sub-vertical, low-amplitude zones that disrupt stratigraphic reflections (e.g., Figs 2A and B). These dike-related zones are >100 m wide (Fig. 2A), but borehole data suggests dike thicknesses may only be 10’s of metres (Magee and Jackson, 2020); i.e. the width of a dike’s seismic expression may not capture its true thickness. The radial geometry of the swarm suggests dikes propagated laterally northwards (Fig. 2A) (Magee and Jackson, 2020). Above and parallel to the dikes are graben bound by normal faults that converge on the upper tips of underlying dikes (Figs 2B and C). The faults displace a ~1 km of Triassic-to-Jurassic strata (Fig. 2B), which locally comprises interbedded claystones, siltstones, and sandstones (Ellis, 2011). At their upper tips, dike-induced faults offset the ~148 Myr base-Cretaceous unconformity (horizon HK; Fig. 2B), which marks the syn-faulting free surface and indicates diking occurred during minor Tithonian rifting (Magee and Jackson, 2020).

We examined an ~18 km long section of a graben bound by faults EF1 and EF2, and underlain by Dike E, imaged in the time-migrated Chandon 3D seismic reflection survey (Fig. 2). Both EF1 and EF2 are continuous along-strike and rarely intersect pre-existing tectonic normal faults (Fig. 2C). Using velocity data from four boreholes and dominant frequency measurements, extracted from the seismic data, we (Supplementary Fig. S2, Table S1, and Table S2): (1) converted the data from depth in time to metres; and (2) estimate the limits of separability (~20±4 m) and visibility (~3±1 m), which define the data's spatial resolution. We mapped 11 seismic horizons (HA–HK; Fig. 2B) and identify their hanging wall and footwall fault cut-offs along 121 transects spaced 125 m apart and oriented orthogonal to EF1 and EF2 (Supplementary Text S1, Fig. S3, and Table S3). For each cut-off pair we measured fault throw and heave, which we use to calculate fault dip and displacement (Supplementary Files 6-8). Along 60 of the transects, spaced 250 m apart, we also measured graben half-width at horizon HF, dike upper tip depth beneath horizon HF, and the width of Dike E's seismic expression at ~4 km depth (Supplementary Text S1, Fig. S3, and Table S3).

GRABEN HALF-WIDTH AND DIKE DEPTH

Graben half-widths (*HW*) measured at the surface are often used to predict dike upper tip depths (*D'*) by assuming fault dip (α) remains constant with depth (i.e. $D' = HW \tan \alpha$) (e.g., Pollard et al., 1983; Trippanera et al., 2015b; Hjartardóttir et al., 2016). We show *HW* along horizon HF is 366±18–728±36 m (Fig. 3A). Using *HW* and by projecting both faults straight down-dip at an angle of HFα (i.e. the average dip at horizon HF for EF1 and EF2), we predict *D'* is 343±51–803±121 m (Fig. 3B). We also measure the depth of Dike E's upper tip beneath horizon HF (*D*), showing it is 493±80–896±134 m (Fig. B). *HW* and *D* are broadly positively correlated, with our data showing that *D* typically exceeds ($D':D < 0.9$) but is locally equal ($D':D = 0.9$–1.1) or less ($D':D > 1.1$) than *D'* (Figs 3B and C).

The discrepancies between *D* and *D'* (Figs 3B and C) may relate to the: (1) true location of Dike E's upper tip being shallower than resolved, such that our measurements overestimate *D*; and/or (2) down dip variations in α (Fig. 3D). Where $D':D$ is <0.9, α for EF1 and EF2 broadly decreases below horizon HF and the faults display convex-up (listric) geometries (Figs 3C and E). Conversely, where α remains constant with depth or increases below horizon HF (i.e. faults are concave-up), $D':D$ is >0.9 (Figs 3C and E). The variation in α across EF1 and EF2 may reflect modification of dike-induced stresses by stresses related to pre-existing tectonic faults (e.g., Fig. 3A), and/or heterogeneity in the mechanical properties of the layered, sedimentary host rock (e.g., Schöpfer et al., 2006; Bazargan and Gudmundsson, 2019). Our results imply graben half-width cannot be used to accurately predict dike upper tip depths without information on subsurface fault structure and host rock lithological variation (cf. Wilson and Head, 2002; Trippanera et al., 2015b; Hjartardóttir et al., 2016).

DIKE-INDUCED FAULT DISPLACEMENTS AND KINEMATICS

Dike-induced fault displacement is intrinsically linked to dike dilation, implying the at-surface 'cumulative heave' (extension) of dike-induced fault pairs can be related to dike thickness (e.g., Rubin and Pollard, 1988; Rubin, 1992; Trippanera et al., 2015b). However, fault heave is also dependent on variations in fault dip and displacement. We measure the cumulative heave of EF1 and EF2 at the syn-faulting free surface (i.e. horizon HK; Magee and Jackson, 2020), and determine their 'total extension'; i.e. the sum of maximum heave values for both faults measured at *any* structural level on each transect (Supplementary Fig. S3). By comparing these measurements to fault dip, displacement distribution, and the width of Dike E's expression, we test whether at-surface cumulative heave measurements reflect dike thickness.

We show fault dip and displacement vary across EF1 and EF2, with both faults displaying zones of elevated displacement (e.g., EF2 segments 1–3) (Figs 3B and 4A). Displacement maxima measured on each transect (~78±12 m on EF1; ~101±15 m on EF2) occur at various structural levels (Fig. 4A); i.e. displacement-depth profiles are more complex than hypothetical models predict (cf. Figs 1 and 4B). Overall, displacement broadly decreases northwards (Fig. 4A). The total extension accommodated by the dike-induced faults mimics the displacement distribution and broadly decreases northwards (Fig. 4C). This northwards decrease in displacement and total extension coincides with a reduction in the width of Dike E's seismic expression (Figs 4A and B). In contrast, the distribution of cumulative heave across horizon HK does not correlate with variations in the total extension or Dike E width, showing no clear northwards decrease (Fig. 4B). There is also no correlation between fault dip, cumulative heave, or total extension (Fig. 4C; Supplementary Fig. S4).

Assuming the northwards reduction in the width of Dike E's seismic expression relates to changes in its true thickness (Magee and Jackson, 2020), the coincident northwards decrease in total extension (and displacement) may be considered a proxy for dike thickness

(Fig. 4B). Local variations in total extension and displacement superimposed onto this northwards decrease, which do not relate to changes in fault dip, could reflect processes controlling dike thickness *during* or *after* emplacement (e.g., thermal wall rock erosion; Fig. 4D) (e.g., Delaney and Pollard, 1981; Gudmundsson, 1983; Kavanagh and Sparks, 2011; Gudmundsson et al., 2012; Rivalta et al., 2015; Vachon and Hieronymus, 2017). An alternative interpretation is that the zones of elevated displacement and total extension correspond to fault nucleation sites (e.g., Pollard and Segall, 1987; Trippanera et al., 2015b; Deng et al., 2017), with the distribution of these zones across EF1 and EF2 suggesting (Figs 4A-C and E): (1) isolated fault segments nucleated and eventually linked (e.g., Willemse et al., 1996), perhaps due to cyclical phases of dike propagation and stalling (e.g.,Woods et al., 2019); and (2) segment nucleation primarily occurred between the dike upper tip and the contemporaneous surface (e.g., Mastin and Pollard, 1988; Koehn et al., 2019), with few nucleating at the dike upper tip (cf. Rubin, 1992; Xu et al., 2016; Koehn et al., 2019) or the syn-faulting free surface (cf. Trippanera et al., 2015a; Trippanera et al., 2015b; Al Shehri and Gudmundsson, 2018). Similar to controls on fault dip variation, fault displacement distribution may have been influenced by the mechanically layered stratigraphy and/or stresses related to pre-existing tectonic faults (e.g., Schöpfer et al., 2006).

Our results show cumulative heave measured at the syn-faulting free surface (i.e. horizon HK) does not equal or mimic the total extension across EF1 and EF2, nor does it reflect the broad northwards decrease in the width of Dike E’s expression (Fig. 4B), implying it is not a proxy for dike thickness (cf. Rubin and Pollard, 1988; Rubin, 1992; Trippanera et al., 2015b). The lack of correlation between fault dip and cumulative heave suggests, instead, that the latter is likely controlled by the vertical distribution of displacement during fault linkage and/or dike thickening-related fault slip (Figs 4D and 4E).

CONCLUSIONS

We use 3D seismic reflection data to image graben-bounding, dike-induced faults that extend downwards from the syn-faulting free surface to converge on the upper tip of a dike. Our results demonstrate predicted dike upper tip depths, calculated from graben half-width and assuming faults are planar, consistently underestimates measured dike upper tip depths. This disparity between predicted and measured dike upper tip depths occurs because fault dip varies down-dip, which possibly reflects heterogeneity in the mechanical properties of the sedimentary host rock and/or stresses around pre-existing tectonic faults. We also show displacement varies across the dike-induced faults, defining zones of elevated displacement. If these zones of elevated displacement correspond to fault nucleation sites, their distribution implies most fault segments nucleated *between* the dike upper tip and free surface. Because the displacement maxima rarely occur at the fault upper tips, our measurements of fault heave along the syn-faulting surface do not approximate dike thickness.

Accurately constraining dike parameters (e.g., thickness and depth) from the surface expression of dike-induced faults requires knowledge of fault geometry and kinematics in 3D. Reflection seismology is a powerful tool for studying how faults grow above dikes, and we anticipate future seismic-based studies will improve our understanding of how diking translates into surface deformation.

ACKNOWLEDGEMENTS

CM is funded by the U.K. Natural Environment Research Council (NERC) Independent Research Fellowship (NE/R014086/1). We thank Geoscience Australia for the publicly available data (http://www.ga.gov.au/nopims) and Schlumberger for Petrel software. We thank M. Townsend, A. Gudmundsson, J. Bull, C. von Hagke, and four anonymous reviewers for constructive comments.

FIGURE CAPTIONS

Figure 1: Half-space schematics showing dike-induced fault growth models (based on Mastin and Pollard, 1988; Rubin and Pollard, 1988; Tentler, 2005; Trippanera et al., 2015b; Koehn et al., 2019); thick black lines mark faults, with arrows marking the downthrow direction, and thin black lines represent stratigraphic horizons. We predict displacement-depth profiles for each model assuming displacement is greatest where faults nucleate (e.g., Pollard and Segall, 1987; Deng et al., 2017); stars highlight displacement maxima and white circles are displacement minima. Horizontal stress patterns above an intruding dike, showing concentrated tensile stress at the surface (i) and above the dike tip (ii), are included (Rubin and Pollard, 1988).

Figure 2: (A) Root-mean squared (RMS) amplitude extraction from seismic data across a 0.2 km high window centred at 4 km depth showing dike A–I traces. Four boreholes shown are: 1=Chandon-1; 2=Chandon-2; 3=Chandon-3; 4=Yellowglen-1. Inset: Location map of the Chandon 3D seismic reflection survey and Exmouth Dyke Swarm. (B) Interpreted depth-converted seismic section showing the studied dike-induced faults (EF1 and EF2); see (C) for location and legend, Fig. S1 for uninterpreted version, and Video S1 for a data video. (C) Horizon HF structure map showing dike-induced faults, underlying dike traces, and tectonic faults; see A for latitude and longitude marking (yellow circles) values.

Figure 3: (A) RMS amplitude map of the seismic reflection data and graph showing variations in graben half-width (*HW*) along-strike at horizon HF. Dip variations of both faults at HF (HFα) are highlighted. Error bars for *HW* are ±5% (see Text S1 for explanation of error sources). (B) Plot comparing measured (*D*) and predicted (*D'*) dike upper tip depths below

HF. Error envelopes for *D* and *D'* are ±15%. (C) Variation in the ratio of *D'*:*D* along the graben related to fault dip, where: (i) for *D'*:*D* < 0.9, fault dip decreases with depth; (ii) for *D'*:*D* = 0.9–1.1, the fault is planar; and (iii) for *D'*:*D* > 0.9, fault dip increases with depth. Error envelope is ±15%. (D) Dip map of EF1 and EF2. (E) Fault dips calculated along each measured transect for EF1 and EF2 plotted against their corresponding seismic horizon (i.e. a proxy for depth; horisons are shown in Fig. 2B). Each transect is colored according to its location along the dike length from south (white) to north (dark red). The dip profiles are grouped for *D'*:*D* < 0.9 and *D'*:*D* > 0.9; inset schematics show how changes in fault dip beneath horizon HF impact *D'*:*D* (dike upper tip is shown in red).

Figure 4: (A) Map of displacement and displacement maxima across EF1 and EF2. Displacement maxima are plotted against distance, with error bars of ±15%, and combined to show cumulative maximum displacement. (B) Depth-displacement profiles for EF1 and EF2; error bars are ±15%, and limit of separability (black dashed line and gray envelope) shown. See (A) for locations and Fig. 2B for horizons. (C) Along-strike variations in total extension across EF1 and EF2, compared to cumulative heave at horizon HK and Dike E's seismic expression width measured from Figure 2A; error bars are ±15%, and limit of separability (black dashed line and gray envelope) shown. Average dip of both faults at each site are highlighted. (D) Schematic showing how localized zones of high displacement may form in response to dike thickening. (E) Schematic showing how isolated fault segments may nucleate in response to dike propagation, then grow and link when the dike stalls and thickens (e.g., Woods et al., 2019). Lateral separation of fault segments may reflect magma break-out from the dike nose (Healy et al., 2018).

REFERENCES

Al Shehri, A., and Gudmundsson, A., 2018, Modelling of surface stresses and fracturing during dyke emplacement: Application to the 2009 episode at Harrat Lunayyir, Saudi Arabia: Journal of Volcanology and Geothermal Research, v. 356, p. 278-303.

Bazargan, M., and Gudmundsson, A., 2019, Dike-induced stresses and displacements in layered volcanic zones: Journal of Volcanology and Geothermal Research, v. 384, p. 189-205.

Carbotte, S. M., Detrick, R. S., Harding, A., Canales, J. P., Babcock, J., Kent, G., Van Ark, E., Nedimovic, M., and Diebold, J., 2006, Rift topography linked to magmatism at the intermediate spreading Juan de Fuca Ridge: Geology, v. 34, no. 3, p. 209-212.

Delaney, P. T., and Pollard, D. D., 1981, Deformation of host rocks and flow of magma during growth of minette dikes and breccia-bearing intrusions near Ship Rock, New Mexico: U. S. Geological Survey Professional Paper 1202, p. 1-61.

Deng, C., Gawthorpe, R. L., Finch, E., and Fossen, H., 2017, Influence of a pre-existing basement weakness on normal fault growth during oblique extension: Insights from discrete element modeling: Journal of Structural Geology, v. 105, p. 44-61.

Dumont, S., Klinger, Y., Socquet, A., Doubre, C., and Jacques, E., 2017, Magma influence on propagation of normal faults: Evidence from cumulative slip profiles along Dabbahu-Manda-Hararo rift segment (Afar, Ethiopia): Journal of Structural Geology, v. 95, p. 48-59.

Ellis, C., 2011, Yellowglen 1 Well Completion Report (Interpretative Data): Perth, Chevron, p. 1-528.

Gudmundsson, A., 1983, Form and dimensions of dykes in eastern Iceland: Tectonophysics, v. 95, no. 3-4, p. 295-307.

-, 2003, Surface stresses associated with arrested dykes in rift zones: Bulletin of Volcanology, v. 65, no. 8, p. 606-619.

Gudmundsson, A., Kusumoto, S., Simmenes, T. H., Philipp, S. L., Larsen, B., and Lotveit, I. F., 2012, Effects of overpressure variations on fracture apertures and fluid transport: Tectonophysics, v. 581, p. 220-230.

Hardy, S., 2016, Does shallow dike intrusion and widening remain a possible mechanism for graben formation on Mars?: Geology, v. 44, no. 2, p. 107-110.

Healy, D., Rizzo, R., Duffy, M., Farrell, N. J., Hole, M. J., and Muirhead, D., 2018, Field evidence for the lateral emplacement of igneous dykes: Implications for 3D mechanical models and the plumbing beneath fissure eruptions: Volcanica, v. 1, no. 2, p. 85-105.

Hjartardóttir, Á. R., Einarsson, P., Gudmundsson, M. T., and Högnadóttir, T., 2016, Fracture movements and graben subsidence during the 2014 Bárðarbunga dike intrusion in Iceland: Journal of Volcanology and Geothermal Research, v. 310, p. 242-252.

Kavanagh, J., and Sparks, R. S. J., 2011, Insights of dyke emplacement mechanics from detailed 3D dyke thickness datasets: Journal of the Geological Society, v. 168, no. 4, p. 965-978.

Koehn, D., Steiner, A., and Aanyu, K., 2019, Modelling of extension and dyking-induced collapse faults and fissures in rifts: Journal of Structural Geology, v. 118, p. 21-31.

Magee, C., and Jackson, C.-L., 2020, Seismic reflection data reveal the 3D structure of the newly discovered Exmouth Dyke Swarm, offshore NW Australia: Solid Earth, v. 11, no. 2, p. 576-606.

Mastin, L. G., and Pollard, D. D., 1988, Surface deformation and shallow dike intrusion processes at Inyo Craters, Long Valley, California: Journal of Geophysical Research: Solid Earth, v. 93, no. B11, p. 13221-13235.

Pallister, J. S., McCausland, W. A., Jónsson, S., Lu, Z., Zahran, H. M., El Hadidy, S., Aburukbah, A., Stewart, I. C., Lundgren, P. R., and White, R. A., 2010, Broad accommodation of rift-related extension recorded by dyke intrusion in Saudi Arabia: Nature Geoscience, v. 3, no. 10, p. 705.

Pollard, D. D., Delaney, P. T., Duffield, W. A., Endo, E. T., and Okamura, A. T., 1983, Surface deformation in volcanic rift zones: Tectonophysics, v. 94, no. 1-4, p. 541-584.

Pollard, D. D., and Segall, P., 1987, Theoretical displacements and stresses near fractures in rock: with applications to faults, joints, veins, dikes, and solution surfaces, *in* Atkinson, B., ed., Fracture mechanics of rock: London, Academic Press, p. 277-347.

Rivalta, E., Taisne, B., Bunger, A., and Katz, R., 2015, A review of mechanical models of dike propagation: Schools of thought, results and future directions: Tectonophysics, v. 638, p. 1-42.

Rowland, J., Baker, E., Ebinger, C., Keir, D., Kidane, T., Biggs, J., Hayward, N., and Wright, T., 2007, Fault growth at a nascent slow-spreading ridge: 2005 Dabbahu rifting episode, Afar: Geophysical Journal International, v. 171, no. 3, p. 1226-1246.

Rubin, A. M., 1992, Dike-induced faulting and graben subsidence in volcanic rift zones: Journal of Geophysical Research: Solid Earth, v. 97, no. B2, p. 1839-1858.

Rubin, A. M., and Pollard, D. D., 1988, Dike-induced faulting in rift zones of Iceland and Afar: Geology, v. 16, no. 5, p. 413-417.

Ruch, J., Wang, T., Xu, W., Hensch, M., and Jónsson, S., 2016, Oblique rift opening revealed by reoccurring magma injection in central Iceland: Nature communications, v. 7, p. 12352.

Schöpfer, M. P. J., Childs, C., and Walsh, J. J., 2006, Localisation of normal faults in multilayer sequences: Journal of Structural Geology, v. 28, no. 5, p. 816-833.

Tentler, T., 2005, Propagation of brittle failure triggered by magma in Iceland: Tectonophysics, v. 406, no. 1, p. 17-38.

Trippanera, D., Acocella, V., Ruch, J., and Abebe, B., 2015a, Fault and graben growth along active magmatic divergent plate boundaries in Iceland and Ethiopia: Tectonics, v. 34, no. 11, p. 2318-2348.

Trippanera, D., Ruch, J., Acocella, V., and Rivalta, E., 2015b, Experiments of dike-induced deformation: Insights on the long-term evolution of divergent plate boundaries: Journal of Geophysical Research: Solid Earth, v. 120, no. 10, p. 6913-6942.

Vachon, R., and Hieronymus, C. F., 2017, Effect of host-rock rheology on dyke shape, thickness and magma overpressure: Geophysical Journal International, v. 208, no. 3, p. 1414-1429.

Von Hagke, C., Kettermann, M., Bitsch, N., Bücken, D., Weismüller, C., and Urai, J. L., 2019, The effect of obliquity of slip in normal faults on distribution of open fractures: Frontiers in Earth Science, v. 7, no. 18.

Willemse, E. J., Pollard, D. D., and Aydin, A., 1996, Three-dimensional analyses of slip distributions on normal fault arrays with consequences for fault scaling: Journal of Structural Geology, v. 18, no. 2-3, p. 295-309.

Wilson, L., and Head, J. W., 2002, Tharsis-radial graben systems as the surface manifestation of plume-related dike intrusion complexes: Models and implications: Journal of Geophysical Research: Planets, v. 107, no. E8.

Woods, J., Winder, T., White, R. S., and Brandsdóttir, B., 2019, Evolution of a lateral dike intrusion revealed by relatively-relocated dike-induced earthquakes: The 2014–15 Bárðarbunga–Holuhraun rifting event, Iceland: Earth and Planetary Science Letters, v. 506, p. 53-63.

Xu, W., Jónsson, S., Corbi, F., and Rivalta, E., 2016, Graben formation and dike arrest during the 2009 Harrat Lunayyir dike intrusion in Saudi Arabia: Insights from InSAR, stress calculations and analog experiments: Journal of Geophysical Research: Solid Earth, v. 121, no. 4, p. 2837-2851.

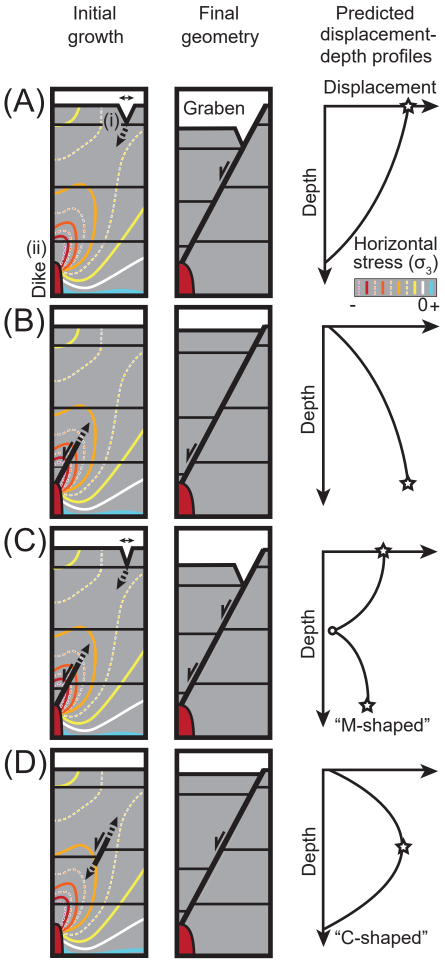
Initial growth
Final geometry
Predicted displacement-depth profiles
(A)
(i)
(ii)
Dike
Graben
Displacement
Depth
Horizontal stress (σ_3)
-
0+
(B)
Depth
(C)
Depth
"M-shaped"
(D)
Depth
"C-shaped"

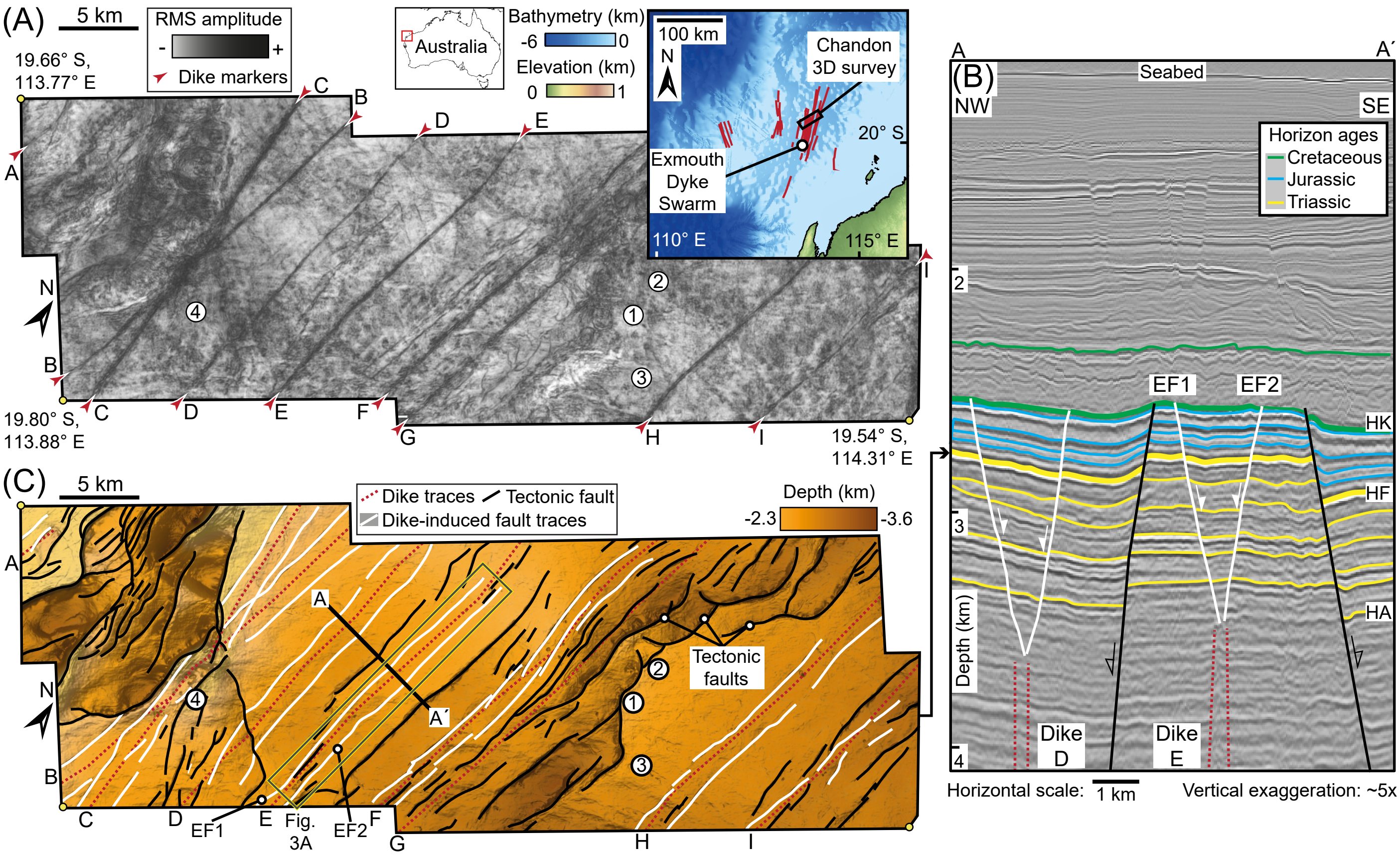
(A)
5 km
RMS amplitude
-
+
Dike markers
Australia
Bathymetry (km)
-6
0
Elevation (km)
0
1
100 km
N
Chandon
3D survey
Exmouth
Dyke
Swarm
20° S
110° E
115° E
19.66° S,
113.77° E
A
B
C
D
E
F
G
H
I
N
①
②
③
④
19.80° S,
113.88° E
19.54° S,
114.31° E
(C)
5 km
Dike traces
Tectonic fault
Dike-induced fault traces
Depth (km)
-2.3
-3.6
A
A´
Tectonic
faults
EF1
Fig.
3A
EF2
(B)
A
A´
Seabed
NW
SE
Horizon ages
Cretaceous
Jurassic
Triassic
2
3
4
Depth (km)
EF1
EF2
HK
HF
HA
Dike
D
Dike
E
Horizontal scale:
1 km
Vertical exaggeration: ~5x

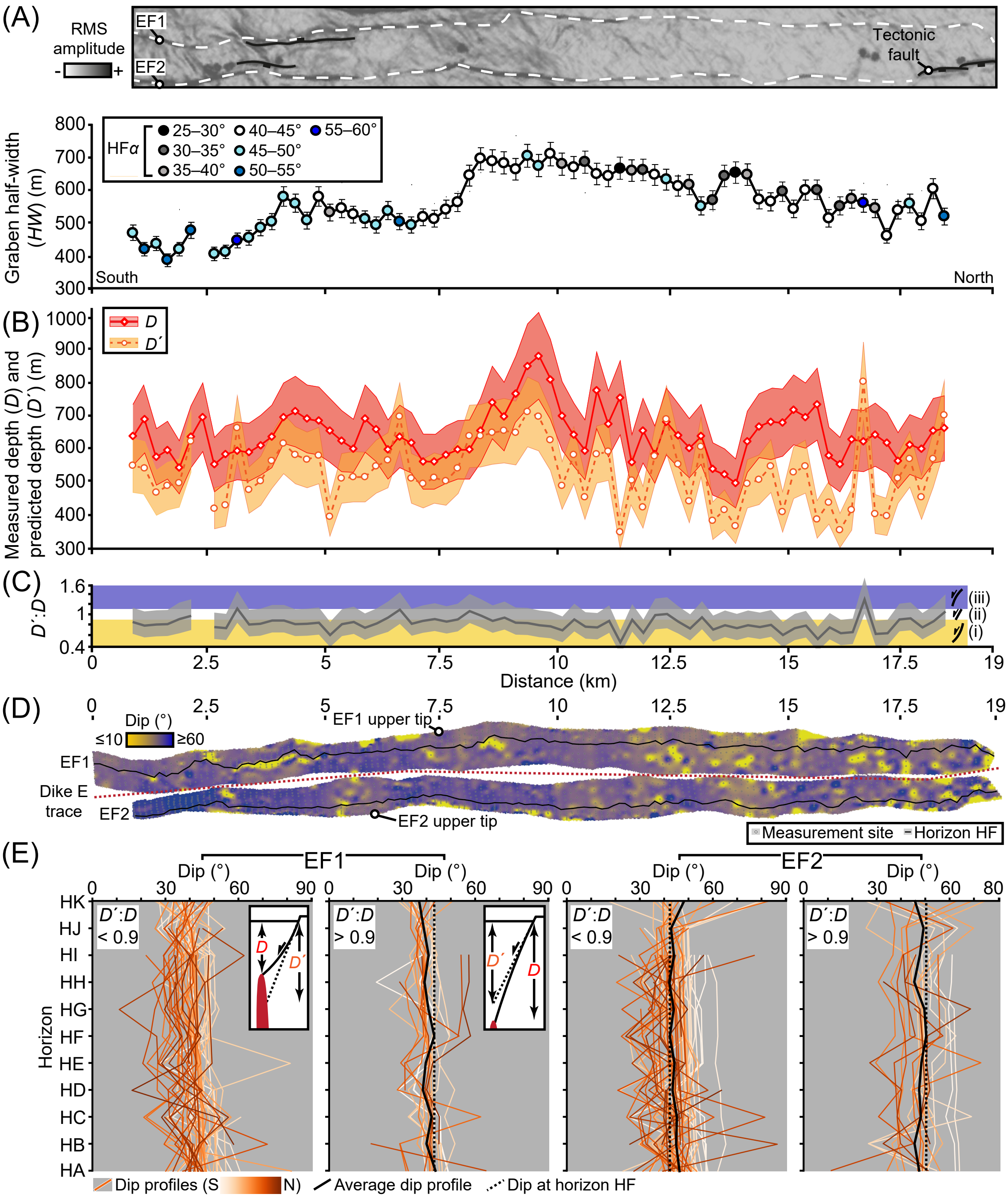
(A)
RMS amplitude
- +
EF1
EF2
Tectonic fault
Graben half-width (HW) (m)
800
700
600
500
400
300
HFα
25–30°
30–35°
35–40°
40–45°
45–50°
50–55°
55–60°
South
North
(B)
Measured depth (D) and predicted depth (D´) (m)
1000
900
800
700
600
500
400
300
D
D´
(C)
D´:D
1.6
1
0.4
(iii)
(ii)
(i)
0
2.5
5
7.5
10
12.5
15
17.5
19
Distance (km)
(D)
Dip (°)
≤10
≥60
EF1 upper tip
EF1
Dike E trace
EF2
EF2 upper tip
Measurement site
Horizon HF
(E)
EF1
EF2
Dip (°)
0
30
60
90
80
HK
HJ
HI
HH
HG
HF
HE
HD
HC
HB
HA
Horizon
D´:D < 0.9
D´:D > 0.9
D
D´
Dip profiles (S N)
Average dip profile
Dip at horizon HF

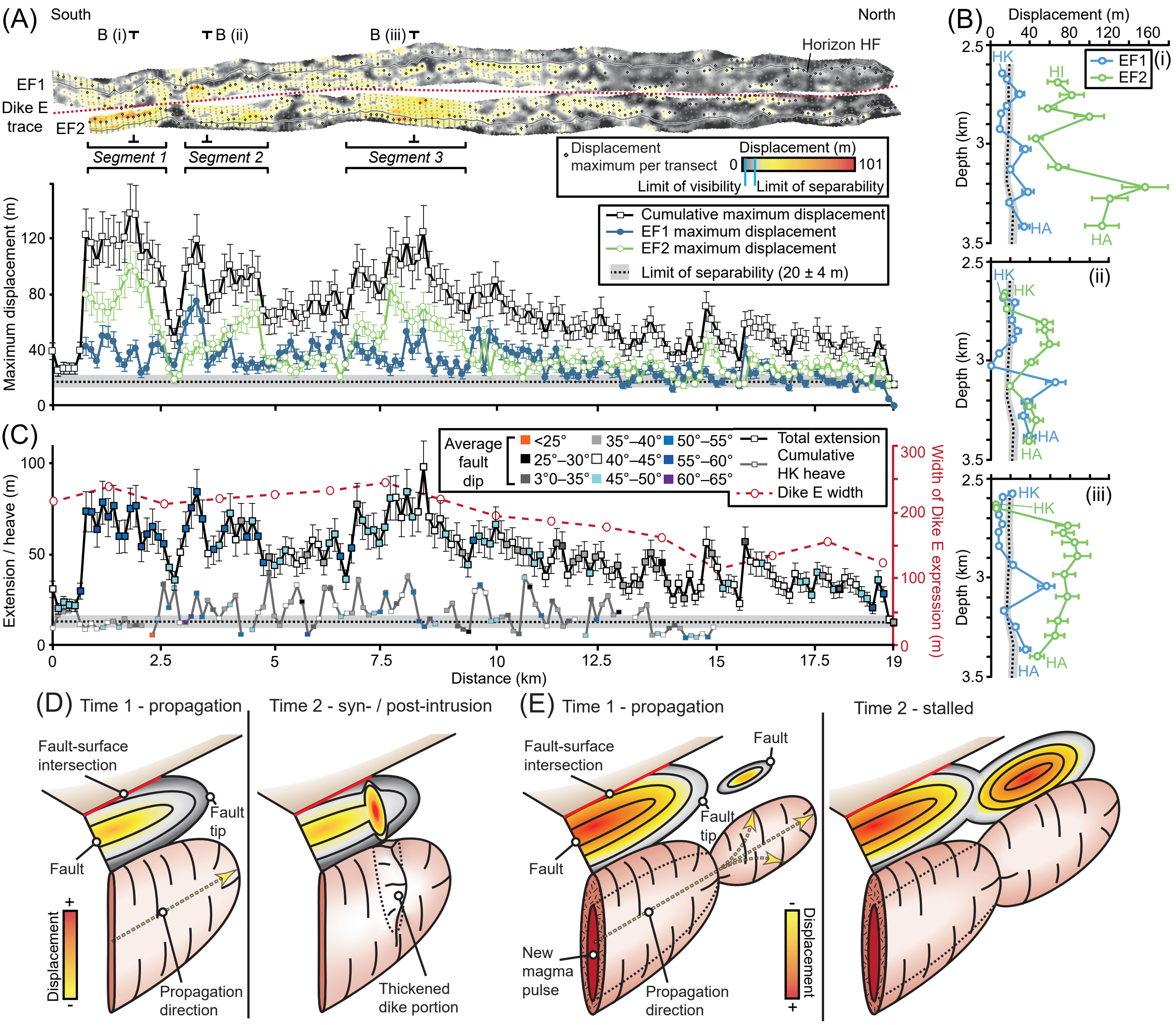
(A)
South
North
B (i)
B (ii)
B (iii)
Horizon HF
EF1
Dike E
trace
EF2
Segment 1
Segment 2
Segment 3
Displacement maximum per transect
Displacement (m)
0
101
Limit of visibility
Limit of separability
Maximum displacement (m)
0
40
80
120
Cumulative maximum displacement
EF1 maximum displacement
EF2 maximum displacement
Limit of separability (20 ± 4 m)
(B)
Displacement (m)
0
40
80
120
160
2.5
3
3.5
Depth (km)
HK
HI
HA
EF1
EF2
(i)
(ii)
(iii)
(C)
Extension / heave (m)
0
50
100
Average fault dip
<25°
25°–30°
3°0–35°
35°–40°
40°–45°
45°–50°
50°–55°
55°–60°
60°–65°
Total extension
Cumulative HK heave
Dike E width
Width of Dike E expression (m)
0
100
200
300
Distance (km)
0
2.5
5
7.5
10
12.5
15
17.5
19
(D)
Time 1 - propagation
Time 2 - syn- / post-intrusion
Fault-surface intersection
Fault tip
Fault
Displacement
+
-
Propagation direction
Thickened dike portion
(E)
Time 1 - propagation
Time 2 - stalled
Fault-surface intersection
Fault
Fault tip
New magma pulse
Propagation direction
Displacement
-
+